Design Principles for Transpiration Cooled Ceramic Sharp Leading Edges

Tobias Hermann*, Matthew McGilvray†, Raghul Ravichandran‡, Marc Ewenz Rocher§
Oxford Thermofluids Institute, University of Oxford, Oxford, OX2 0ES, United Kingdom

Madeleine Grossman¶, Luc Vandeperre‖
Dept. of Materials, Centre for Advanced Structural Ceramics, Imperial College London, London, SW7 2AZ, United Kingdom

Transpiration cooling is an active methodology in reducing surface heat flux for hypersonic vehicles, which offers the possibility of reducing nose bluntness and therefore increasing aerodynamic performance. This paper presents a numerical analysis of transpiration cooled sharp leading edges made from ultra-high-temperature ceramics (UHTCs). The structural integrity of a 10 mm radius wedge leading edge is investigated numerically with regard to different coolant plenum geometries and pressurisation magnitudes. It is found that the close spacing of individual plenum chambers reduces the stress in the material significantly and provides the maximum possible coolant mass flux. An optimisation procedure of plenum pressure distribution is carried out using an analytical description of the porous flow in the leading edge. It is found that there exists an optimum plenum pressure that minimises the probability of failure of the leading edge model. Nitrogen coolant requires less pressure than Helium to reach this criterion and furthermore requires less pressure to displace the air freestream and thus protect the leading edge from oxidation.

Nomenclature

Latin letters

B_m = mass blowing parameter

B_n = empirical parameter

c = mass fraction

c_p = specific heat

*Associate Professor, Oxford Thermofluids Institute, University of Oxford, AIAA Senior Member. Corresponding author. tobias.hermann@eng.ox.ac.uk

†Professor, Oxford Thermofluids Institute, University of Oxford, AIAA Associate Fellow.

‡DPhil student, Oxford Thermofluids Institute, University of Oxford, AIAA Member.

§DPhil student, Oxford Thermofluids Institute, University of Oxford, AIAA Member.

¶Research Associate, Dept. of Materials, Centre for Advanced Structural Ceramics.

‖Professor, Dept. of Materials, Centre for Advanced Structural Ceramics.

D = diffusivity

E = Young's modulus

F = blowing ratio

h = enthalpy

h_v = volumetric heat transfer coefficient

k = thermal conductivity

K_D = Darcy permeability

K_F = Forchheimer permeability

$\dot{m}$ = mass flux

M = molecular weight

N = transformed arc-length

n = iteration parameter

p = pressure

PoF = probability of failure

$\dot{q}$ = heat flux

r = radius

R_N = Vehicle nose radius

Re = Reynolds number

Sc = Schmidt number

s = distance from injector

T = temperature

t = time

$\frac{\mathrm{d}u_e}{\mathrm{d}x}$ = velocity gradient

v = velocity

V = volume

W = width of injector

w = width of plenum

Y = mole fraction

Greek letters

α = coefficient of thermal expansion

ϵ = emissivity

η = film effectiveness

ϕ = porosity

μ = dynamic viscosity

ν = Poisson's ratio

ρ = density

σ_c = principal stress

θ = cylinder angle

ξ = transformed x variable

Ω = solid angle

Subscripts

s = solid material

f = fluid

c = coolant

g = external gas

w = wall / surface

e = boundary layer edge

∞ = freestream conditions

r = recovery conditions

i = injection conditions

$*$ = evaluated at reference temperature T^*

inj = injected coolant

Air = freestream air

coolant = coolant species

stag = stagnation point

surface = surface condition

I. Introduction

Hypersonic vehicles are exposed to extreme surface heat fluxes due to the conversion of kinetic energy into internal energy of their surrounding gas [1]. The bow shock in front of a vehicle compresses the freestream gas and leads to a large increase in static pressure and temperature which in turn create large surface heat fluxes through convection. These heat fluxes are driven by the magnitude of the temperature gradient at the vehicle's surface, which become larger for a

thinner boundary layer. For a cylindrical or spherical leading edge, the boundary layer can be regarded as self-similar, i.e. the boundary layer thickness scales with the leading edge radius. Thus, a smaller leading edge radius leads to a thinner boundary layer which also amplifies the heat transfer by creating a larger temperature gradient at the surface. Many studies have produced analytical or semi-empirical correlations for this behaviour [2, 3].

The described effects are the reason why blunt bodies have been used historically for vehicles that travel at speeds that would lead to exorbitant heat fluxes for sharp leading edges. This phenomenon creates a limited flight condition corridor for slender vehicles with sharp leading edges. These vehicles have desirable aerodynamic characteristics, such as better manoeuvrability and less drag, which makes them a sought after alternative to blunt bodies. Modern materials are envisaged to enable the use of active cooling techniques to extend the operational flight conditions that can be achieved with sharp leading edges [4–6]. This paper investigates the use of transpiration cooling as a means to achieve this. Transpiration cooling is the passing of a relatively cool fluid through a porous external wall which leads to a cooling of the vehicle [7, 8]. The convective heat transfer between coolant and porous material, the local blockage of external hot gas reaching the surface, and the establishment of a protective film are the mechanisms that reduce the net surface heat flux. The effectiveness and fundamental fluid mechanics of transpiration cooling have been investigated in depth over the last few decades, building a strong case for the potential of an active cooling system [9–14]. However, very few flight missions have actually used the technique, as the complexity of the system is high and, by virtue of being a thermal protection system, it represents a single point of failure. What transpiration cooling offers as a unique benefit compared to other thermal protection systems, is shape stability and re-usability. The development of modern high-temperature porous materials enables a new look into this unique advantage over other systems, through employing hybrid manufacturing techniques to achieve complex geometric structures. The key factors are materials that stay inert at extreme temperatures and retain sufficient mechanical strength at flight conditions. A schematic drawing of a transpiration cooled leading edge is shown in Fig. 1.

This work focuses on one such option which employs ultra-high-temperature ceramics (UHTCs) as a material choice due to their very high melting point, their isotropic properties, and their relatively stable material properties at high temperatures. Modern manufacturing techniques, such as gelcasting, robocasting, and partial sintering enable a large design space in terms of achievable geometries and material properties [15]. This makes these materials a strong candidate for future transpiration cooled systems. The drawback of UHTCs is the vulnerability to oxidation at elevated temperatures. In addition, an actively cooled leading edge is faced with a number of additional challenges: The large gradients in surface pressure around the vehicle have a significant influence on the porous flow within the leading edge, thus changing the mass injection distribution. Similarly, the large heat flux gradients require more mass injection at the stagnation point, which complicates the porous flow inside the material even further. The heat flux distribution will also change the local coolant viscosity in the material which affects the preferential flow path. Hence, the design of a real system is faced with a highly coupled system between external aerodynamic properties, heat transfer, and porous flow.

Even with these aspects considered, it begs the question how to introduce the coolant in a way that also retains maximum structural integrity of the system and provides the required coolant injection. Previous system studies have focused on the effectiveness in terms of heat flux mitigation or heat transfer within the vehicle structure [8, 16, 17]. However, the coupled nature of a pressurised plenum, porous medium, thermal and mechanical stress, and external coolant film in a high-enthalpy flow leads to a multi-physics problem which restricts the practical operational corridor for transpiration cooled vehicles. The purpose of this work is to establish a methodology to assess the suitability of a design in this highly coupled problem, and to identify principles that lead to favourable architectures. The plenum architecture, which is left blank in Fig. 1, will be a particular focus of the current paper. A numerical methodology is described comprised of simulations of the flow, porous medium, and mechanical and thermal stress of the vehicle structure. Results of different canonical structural architectures are presented, where both external heat flux and plenum pressure are varied. These results are analysed using a probabilistic failure model of the ultra-high-temperature ceramic structure.

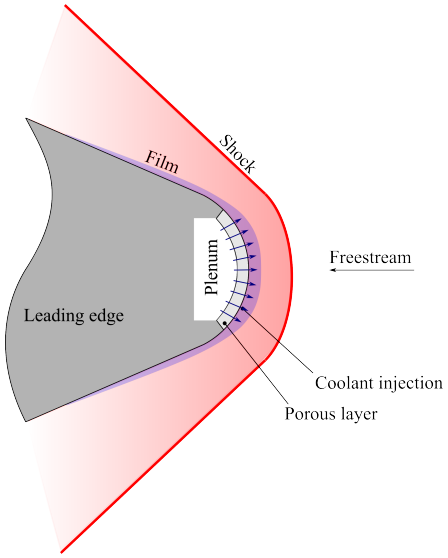

Fig. 1 Schematic of transpiration cooled leading edge in hypersonic flow.

II. Simulation Methodology

The overall goal is to generate optimised cooling conditions for each case investigated in this study, and to then determine the probability of structural failure for this optimised case. Geometries of consideration consist of cylindrically blunted leading edges for two-dimensional wedge geometries. An example of such a geometry is shown in Fig. 2, where the top half is shown, consisting of several plenums and a relatively thin porous injector. The analysis of the leading edge system builds on a number of different numerical tools, owing to the high degree of coupling of the system. Figure 3 shows an overview of the different tools used in this study and the spatial domains where they are employed. In the following, each tool is described.

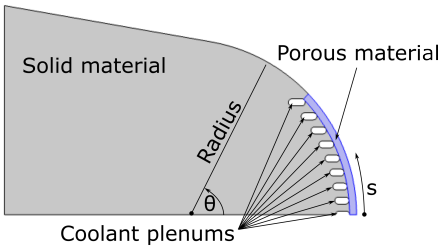

Fig. 2 Half of example leading edge consisting of solid material (grey), porous material (blue) and several void plenums (white).

A. PIRATE

PIRATE is a simulation tool designed for rapid system level studies of transpiration cooled structures. Inputs to PIRATE are the flight velocity and altitude, the material and coolant properties, plenum pressure, and geometry. The tool then determines the temperature distribution and coolant injection mass flux at the surface of the porous medium. This is used either as a straightforward predictive simulation when a defined plenum pressure is given, or as an optimisation tool where the plenum properties are adjusted in order to generate a required mass injection distribution to keep the material temperature below a critical value. This strategy has been extensively used in Ref [17]. The simulation output considered in this study is the coolant mass flux distribution along the leading edge surface. PIRATE is based on semi-empirical correlations describing the external flow properties and uses a convolution approach to determine the heat transfer within a porous medium. The detailed description and validation of the code is presented in Ref. [18]. PIRATE employs the Sutton-Graves stagnation point heat transfer correlation [19]

$$\dot{q}_{\mathrm{S-G,\,stag}} = 1.7415 \cdot 10^{-4} \cdot \left(\frac{\rho_\infty}{R_N}\right)^{0.5} \cdot v_\infty^3 \cdot \left(1 - \frac{h_{\mathrm{surface}}}{h_\infty}\right), \tag{1}$$

with the free stream density, ρ_∞, the free stream velocity, v_∞, the nose radius, R_N. The wall and free stream enthalpies, h_{surface}, and, h_∞, are determined via a chemical equilibrium analysis using the respective pressure and temperature values [20]. The off-stagnation point heat flux along the body is determined using the correlation developed by Lees [21]. Heat flux reduction due to film cooling effects downstream of injection locations is accounted for by utilising the models of Kays et al. [2], Goldstein and Jabbari [7], Kutateladze [22], and Sellers [23]. The external pressure distribution at the vehicle surface is calculated using post-shock chemical equilibrium and a Newtonian pressure distribution [1, 20]. The detailed implementation is documented in [18].

The temperature inside the porous domain is calculated through a quasi one-dimensional approach with a correction

for lateral heat transfer. The governing equations considered are the energy equations of the solid and fluid phase:

$$(1-\phi)\,\rho_s c_{p,s}\frac{\partial T_s}{\partial t} = k_s\,(1-\phi)\,\frac{\partial^2 T_s}{\partial x^2} + k_s\,(1-\phi)\,\frac{\partial^2 T_s}{\partial y^2} + h_v\left(T_f - T_s\right) \tag{2}$$

and

$$\phi\rho_f c_{p,f}\frac{\partial T_f}{\partial t} = \phi\rho_f c_{p,f}\frac{v_f}{\phi}\frac{\partial T_f}{\partial y} + h_v\left(T_s - T_f\right), \tag{3}$$

with (s) denoting the solid phase, (f) denoting the fluid phase, the thermal conductivity, k, the porosity, ϕ, the volumetric heat transfer coefficient, h_v, the time, t, the in-depth location, y, measured from the surface, and the lateral location, x. This formulation assumes one-dimensional flow, and two-dimensional heat transfer. The detailed implementation and validation of this approach is documented in Ref. [16].

PIRATE utilises an impulse response convolution approach to solve Eqs. (2) and (3). The thermal boundary condition at the vehicle surface is the net heat flux of aerodynamic heating and radiative cooling. The boundary condition at the plenum side is the net heat flux of radiative cooling and reflected radiation inside the plenum [18].

A new addition to PIRATE used in this study is the incorporation of a model that accounts for the surface concentration of coolant and freestream air respectively. The implementation of this model is described in the following.

1. Coolant wall concentration

Mass injection through a porous medium creates a coolant film at the vehicle's surface that blocks external gas. However, the momentum of the injected fluid is balanced by the diffusive flux of air through the film. This leads to finite concentration of air at the vehicle's surface, that cannot be eliminated completely. In Ref [24], a semi-empirical model was established to describe this effect. The model is based on classical film theory and uses self-similar boundary layer theory to derive parameters used in the correlation. The implicit equation

$$c_{\text{coolant,blowing}} = 1 - \frac{B_m c_{\text{coolant,blowing}}}{\exp\left(B_m c_{\text{coolant,blowing}}\right) - 1} \tag{4}$$

is used to determine the coolant mass fraction, $c_{\text{coolant,blowing}}$ at the vehicle stagnation point. The parameter B_m is calculated as

$$B_m = \sqrt{\frac{8}{\rho_e \mu_e \frac{\mathrm{d}u_e}{\mathrm{d}x}}} \cdot Sc_{\text{w,Air}}^{0.6} \cdot \dot{m} \cdot \left(\frac{M_{\text{Air}}}{M_{\text{inj}}}\frac{D_{\text{Air}}}{D_{\text{inj}}}\right)^{0.75} \tag{5}$$

with boundary layer edge viscosity μ_e, density, ρ_e, velocity gradient, $\frac{\mathrm{d}u_e}{\mathrm{d}x}$, Schmidt number, $Sc_{\text{w,Air}}$, injection mass flux, $\dot{m}$, freestream molecular weight, M_{Air}, coolant molecular weight, M_{inj}, freestream diffusivity, D_{Air}, and coolant diffusivity, D_{inj}.

The model is utilised to determine the air wall concentration as this is a critical parameter to assess the effectiveness

of transpiration cooling as a means to protect the surface from oxidation. The presence of a film will also decrease the amount of air present at the surface downstream of an injection point. In order to stay consistent with the convective aspect of film cooling implemented in PIRATE, Kutateladze's model is used for concentration as well. This model was originally derived by assuming an instantaneous mixture of the injected coolant and an external boundary layer that develops on the coolant film. The two mixed mass fluxes of coolant and external gas were then used to calculate an average film temperature which was expressed as the film effectiveness η [22]. The same derivation is used for the mass fraction of the mixed film which reduces the correlation to

$$\eta_c = \frac{1}{0.33(4+\xi)^{0.8}}, \qquad \xi = \frac{s_{\text{from injector}}}{F \cdot W}\left(\frac{\text{Re}_f^i \mu_f^i}{\mu^*}\right)^{-0.25}\frac{\rho_g^*}{\rho_g}, \qquad Re_f^i = \frac{\rho_f^i v_f^i W}{\mu_f^i}, \tag{6}$$

with the distance along the vehicle's surface from the injection point, $s_{\text{from injector}}$, the streamwise length of the injector, W, the blowing ratio, F, the dynamic viscosity, μ, and the density ρ [22]. Values denoted by $(*)$ are evaluated at the temperature

$$T^* = 0.28\,T_g + 0.72\,T_{r,g} \tag{7}$$

and the values denoted by (i) are evaluated at the injection temperature, $T_{\text{injected coolant}}$. The calculated film effectiveness downstream is then used as described in Ref [18] to calculate the local coolant mass fraction in the film $c_{\text{coolant,film}}$. Together with the local blowing effect, the combined mixed mass fraction from pre-existing film and local injection is

$$c_{\text{w,Air}} = (1 - c_{\text{coolant,blowing}}) \cdot (1 - c_{\text{coolant,film}}) \tag{8}$$

B. Darcy Flow Model

A simplified analytical model is used to calculate the flow in the porous domain of the leading edge which is described in detail in Ref [25]. The model considers a two-dimensional incompressible Darcy flow through the porous layer. With the boundary conditions of plenum pressure, impermeable sections and the external aerodynamic pressure distribution, the mass flux through the porous material is calculated. The coolant injection velocity at the interface between porous domain and external flowfield is determined via

$$v_r = \frac{B_0}{r} - \sum_{n=1}^{M}\frac{2B_n N}{r^{N+1}}\cos(N\theta) - \frac{K_D}{\mu}\sum_{n=1}^{M}\frac{N}{r}\cos(N\theta)\frac{2}{s}\int_0^s p_e(\theta)\cos(N\theta)\,\mathrm{d}\theta, \tag{9}$$

with $N = (\pi\, n)/s$, arc length along the external surface, s, arc angle, θ, radius, r, Darcy-permeability, K_D, external aerodynamic pressure distribution, p_e, and coefficients, B_n, which are based on the particular boundary conditions.

C. Porous Flow Simulation - SLEDGE

The finite difference tool SLEDGE (Sharp Leading EDge GEometry solver) is used to simulate the flow in a porous medium in steady state. The Darcy-Forchheimer equation for an isotropic medium, and the continuity equations are solved numerically in two dimensions for a compressible fluid using

$$\nabla p = -\frac{\mu}{K_D} v - \frac{\rho}{K_F} v^2 \tag{10}$$

$$\nabla \rho v = 0 \tag{11}$$

, with pressure p, Darcy coefficient K_D, Forchheimer coefficient K_F, viscosity μ, density ρ, and bulk flow velocity v. The ideal gas law is utilised as the corresponding equation of state [26].

An elliptic grid generation according to Anderson [27] is used to transform the two-dimensional Darcy Forchheimer, and mass conservation equations into a Cartesian computational space, where they are solved using a second order finite difference scheme. The boundary conditions include permeable and impermeable sections on the plenum side of the porous domain, and a pressure distribution on the flow-facing side of the porous medium, which is based on the external flow field. These boundary conditions are informed by the respective external flow conditions and the leading edge architecture.

D. Thermo-mechanical simulation - COMSOL

The commercial multiphysics simulation software COMSOL is used to calculate steady state lateral heat conduction and stress fields within the leading edge. The temperature dependence of material properties is also taken into account by accounting for a 1 % decay for every 100 K difference from ambient conditions. The simulated temperature field is used to determine the stresses induced by thermal expansion. In addition, the stress due to the pressurisation of internal plenums or the external aerodynamic force is considered.

E. Structural Probability of Failure Model

A key problem in judging the adequateness of a design for ceramics is that not only the magnitude of the stresses need to be considered but also the volume on which they act as both a large volume and a large stress increase the likelihood that a large enough defect will be present for a crack to propagate. Therefore, finite element analysis to determine maximum stress levels alone is insufficient and further post-processing is required to finally obtain a figure of merit for the design. The methodology that has been chosen to achieve this is one that provides a probability of failure for the design. To account for the three dimensional nature of the stress, a first approximation can be obtained using the Barnett–Freudenthal approximation of treating the principal stresses as three independent cases the material needs to survive, but for the final risk of failure the theory as developed by Batdorf is used, which gives the probability of failure

as

$$PoF = 1 - \exp\left(-\int_V \mathrm{d}v \int_0^\infty \frac{\Omega}{4\pi}\frac{\mathrm{d}N}{\mathrm{d}\sigma_c}\mathrm{d}\sigma_c\right) \tag{12}$$

where Ω is the solid angle of the orientations where the applied equivalent stress is higher than the stress for a crack from the crack distribution N to propagate [28]. Equation (12) is solved numerically by integrating the equation kernel (based on the principal stress fields obtained through the COMSOL simulation) over the entire volume.

F. Optimisation Approach

The simulation and optimisation process employed to investigate the performance of leading edge geometries is shown in Fig. 4, which shows input and output parameters of each step in the simulation methodology. The study considers various different structural architectures featuring different thicknesses of porous material, and varying numbers of plenums. In the following, the simulation steps are enumerated in more detail, and the individual simulation tools are explained. The specific case shown here refers to the conditions summarised in Section III, considering a geometry with a porous layer thickness of 1 mm, a plenum spacing of 0.4 mm, and with a Helium coolant injection.

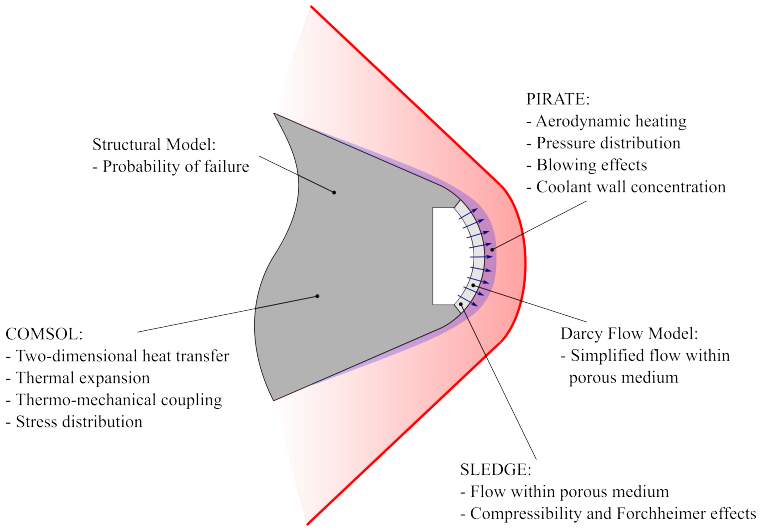

Fig. 3 Tools used to simulate the leading edge.

1) A PIRATE simulation (see Section II.A) is carried out assuming a given flight condition with either Helium or Nitrogen used as coolant. The simulation output is the required mass flux of injected coolant at each location of the surface. The target parameter in this step is to keep the material temperature below 2300 K at every location along the vehicle surface. An example of the required injection mass flux using Nitrogen is shown in Fig. 5. The plot shows the optimised coolant mass flux distribution along the external circumference of the leading edge. Surface length denotes the distance from the stagnation point to the edge of the porous injector piece, at which point the mass flux drops to zero.

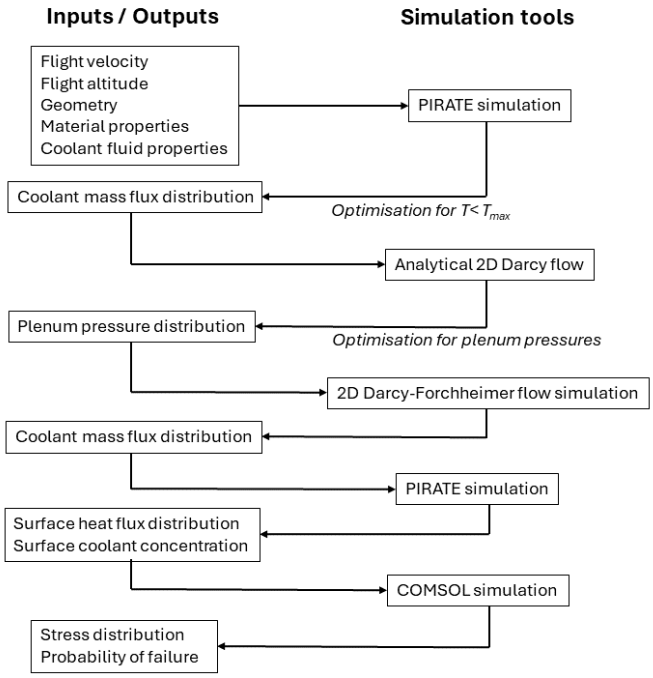

Fig. 4 Flowchart for simulation and optimisation approach.

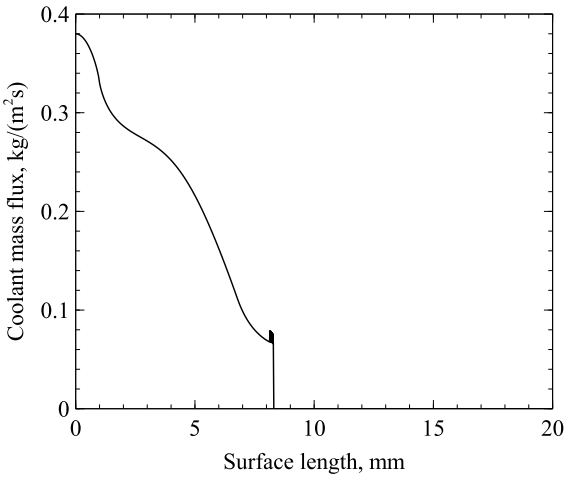

Fig. 5 Target injection mass flux along external surface.

2) The calculated mass flux distribution is the target of this next step, where each plenum pressure is tailored, such that the overall distribution is replicated as closely as possible. For this purpose, the analytical description of Darcy flows (see II.B), is used to optimise the plenum pressure in each individual plenum of a given geometrical configuration. The individual plenum pressures are used as target variables of a non-linear optimisation algorithm where the target mass flux (see Fig. 5) is calculated using the model detailed in Section II.B. An example of the resulting plenum pressure distribution is shown in Fig. 6 with relation to the angle θ as defined in Fig. 2. The red horizontal plateaus are the plenum pressures obtained by the optimisation procedure while the spaces in between,

here labelled as 'impermeable', represent the solid back structure. The plot shows local pressure at the backside of the porous injector, which interfaces with the plenums. Although the optimisation process is of lower fidelity, e.g. incompressible Darcy flow is assumed, the ability to use fast optimisation due to the analytical description of the porous flowfield outweighs the lack of accuracy.

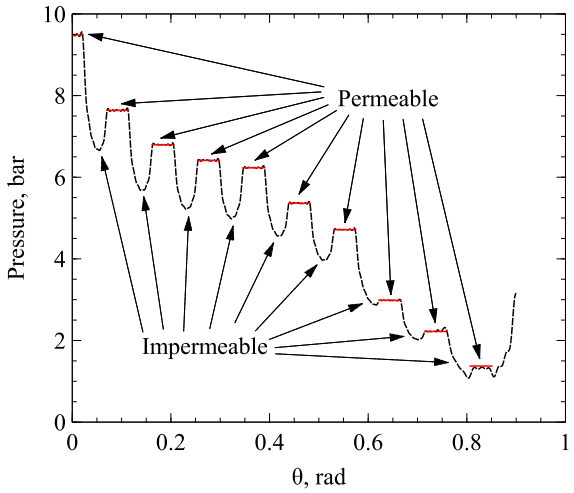

Fig. 6 Pressure at the plenum side from Darcy flow optimization. Red horizontal lines represent plenum locations. By definition, the impermeable regions between plenums do not allow the passing of coolant into the porous domain. However, these regions are still pressurised due to the lateral porous flow originating from adjacent plenums.

3) The next step is a full finite element simulation (FE) of the two-dimensional porous flowfield inside the leading edge. The determined plenum pressures from the previous step are used for internal boundary conditions. The external pressure boundary condition is based on the flight condition and extracted from the PIRATE simulation. This is a pressure distribution along the external surface of the vehicle. The FE simulation is carried out with the in-house code SLEDGE which solves the compressible Darcy-Forchheimer equations (see Section II.C). This provides a higher fidelity than the analytical Darcy flow description, as kinetic Forchheimer effects and compressibility are taken into account. The simulation results in a coolant mass flux distribution at the surface of the leading edge. An example of this is shown in Fig. 7.
4) The next step is to use this mass flux distribution as an input for another PIRATE simulation. The mass flux distribution from step 1 is the ideal target condition, but it can never be fully achieved, as the finite plenum size and the geometry of the porous domain are restricted. Thus, the best fit that can be achieved has to be used as an input parameter to calculate the reduction in heat flux for a real case. This heat flux profile, shown in Fig. 8, is determined through the PIRATE simulation and is subsequently used in the next step.
5) The calculated external heat flux, the external pressure distribution, and the internal plenum pressure distribution are implemented as boundary conditions in a coupled thermo-mechanical COMSOL model (see Section II.D). The model uses these inputs to calculate the two-dimensional distribution of temperature and principal stresses

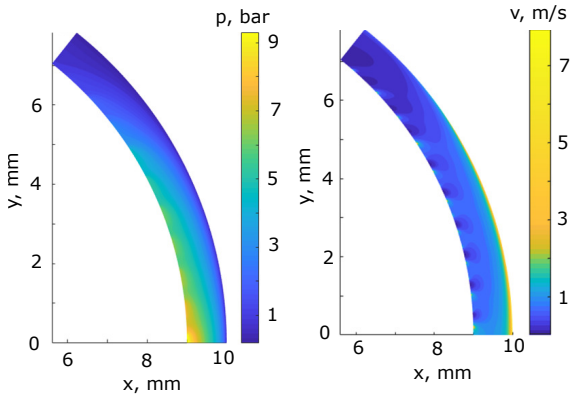

Fig. 7 Porous flowfield after SLEDGE finite element simulation. Left: pressure in bar. Right: Velocity magnitude in m/s**.**

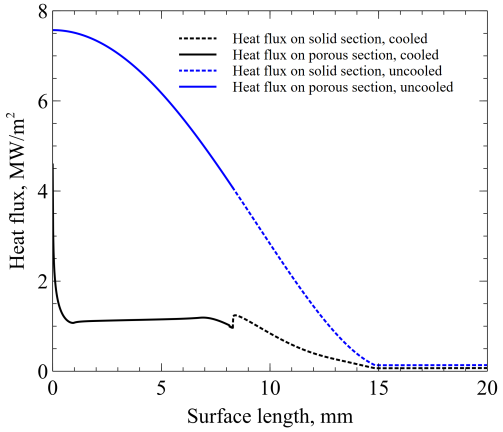

Fig. 8 Original heat flux distribution and cooled heat flux achieved after step 4) in the optimisation procedure outlined in Section II.

in each cell. An example of the first principal stress field is shown in Fig. 9.

6) These stresses are used as input parameters in the probability of failure model (see Section II.E), which employs the Barnett–Freudenthal approximation. The result of this model is an overall probability of failure at the employed plenum pressure and coolant type condition.

The full optimisation procedure takes approximately 16 minutes on an Intel(R) Xeon(R) W-2265 CPU. In the following, each simulation tool is described in greater detail.

III. Test Case

In this study, one flight condition with a velocity of 5.5 km/s at an altitude of 45 km, corresponding to a Mach number of 16.85, is considered which results in a stagnation point heat flux of 7.6 MW/m^2 and a Pitot pressure of 0.47 bar. The flight condition is relevant for boost-glide vehicles and falls within corridors previously investigated in

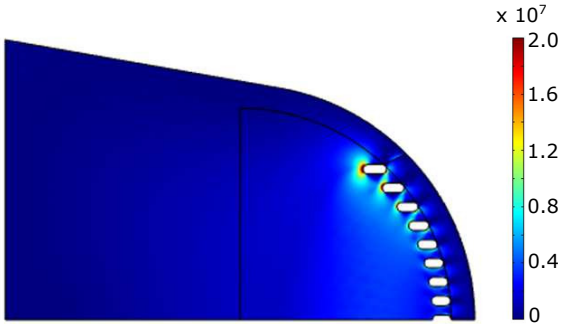

Fig. 9 First principal stress (in Pa) in leading edge geometry.

hypersonic flight system studies [29–31]. The material is taken to be monolithic ZrB_2 with the used material parameters summarised in Table 1 for both porous and solid cases [32–34]. Due to the high stability of thermal and mechanical properties of UHTCs at elevated temperature [35–37], it is assumed that these properties are constant throughout the computational domain. The outer geometry under consideration is a blunt wedge with a full angle of 10 degrees and a nose radius of 10 mm.

The geometries under consideration are shown schematically in Fig. 10. Each case consists of a solid (grey) leading edge body with a porous layer (blue) at the external part of the leading edge near the stagnation point. Due to the large heat flux magnitude in that region and the quick drop as the flow expands around the curved part of the leading edge, cooling is only required close to the stagnation point. The focus of this investigation is how the coolant is best introduced. The approach taken here is the employment of multiple plenum chambers located directly underneath the porous layer. Nine different cooling architectures are investigated that feature different plenum widths and different thicknesses of the porous layer between 0.4 mm and 2.8 mm. The lower boundary of these features is given by current practical manufacturing limits [15]. Each of these geometries includes individual plenum chambers which are separated by solid material that directly attaches to the backside of the porous surface layer. Although these separating walls

Table 1 Material properties of ZrB_2 [32–34].

Property	Porous	Solid
ϕ	40 %	0 %
k	28 W m^{-1} K^{-1}	80 W m^{-1} K^{-1}
c_p	665 J kg^{-1} K^{-1}	665 J kg^{-1} K^{-1}
ρ	3690 kg m^{-3}	5830 kg m^{-3}
E	98 GPa	500 GPa
ν	0.15	0.15
K_D	$2.443 \cdot 10^{-14}$ m^2	0 m^2
K_F	$8.855 \cdot 10^{-8}$ m^{-1}	0 m^{-1}
ϵ	0.75	0.75
α	$7.6 \cdot 10^{-6}$ K^{-1}	$7.6 \cdot 10^{-6}$ K^{-1}

between plenums reduce the permeable surface area on the porous backside, they improve the structural integrity significantly. The increased capability to use higher pressures due to the segmentation of the plenums far outweighs the downside of a smaller porous area. The corner-radius of the plenum chambers has been set to 0.2 mm.

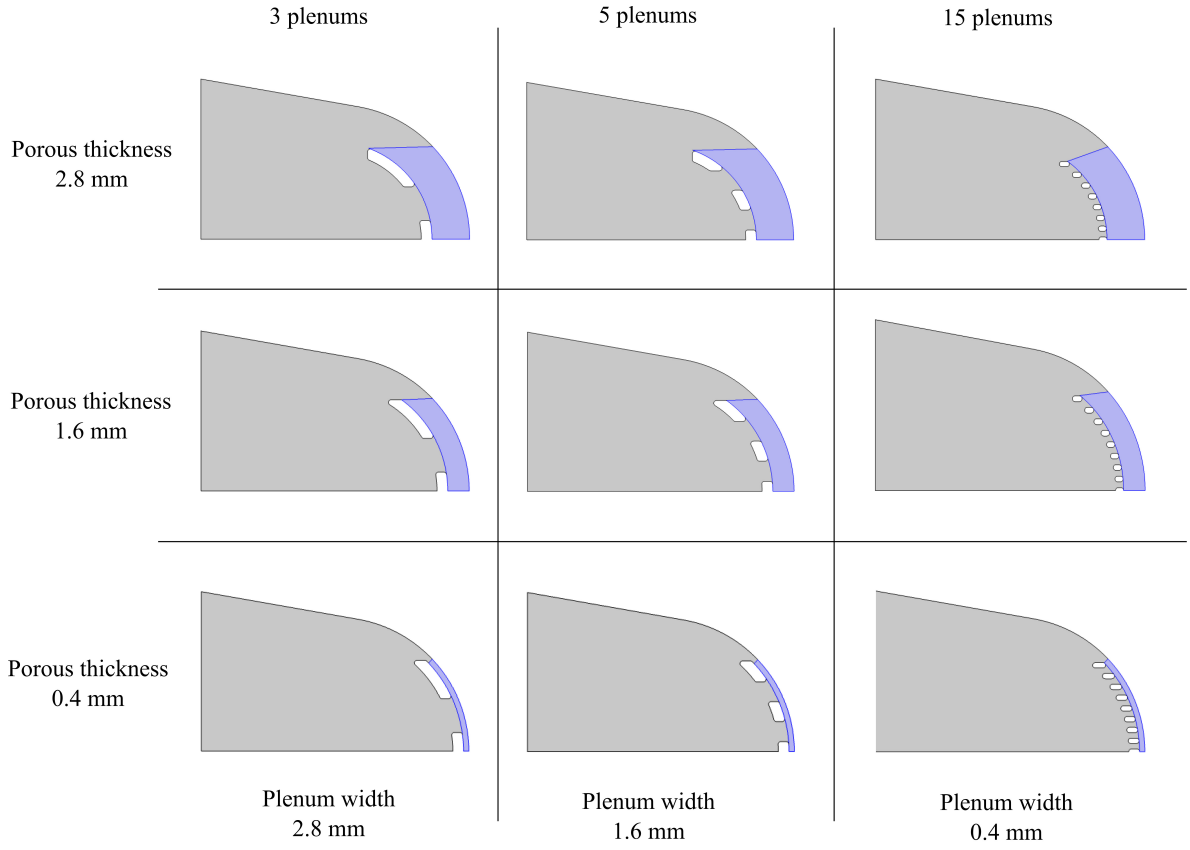

Fig. 10 Halves of leading edge geometries consisting of solid material (grey), porous material (blue) and void plenums (white).

IV. Performance of Plenum Geometries

The first investigation in this study is concerned with the relative performance of different plenum geometries. The investigation carried out in this section forgoes the optimisation approach detailed in Section II, i.e. only purely predictive calculations are performed using pre-determined plenum pressure and heat flux conditions based on the flight condition and material properties detailed in Section III. The external heat and pressure distributions imposed to the external leading edge surface are based on the PIRATE simulation of the flight condition mentioned in Section III. A major problem of UHTCs is the brittle failure that can occur if principal stresses get too high. Mechanical stress is introduced due to thermal expansion causing thermal stress, and due to plenum pressurisation. Therefore, performance is defined in terms of two metrics: A burst mass flux and a burst heat flux. The burst mass flux is the maximum coolant mass flux that can be passed through the leading edge before the component reaches a probability of failure of 1 %. A

higher burst mass flux is desirable as this enables the leading edge to consume more coolant and therefore mitigate more external heat flux. In this section, the burst mass flux is determined in isolation of other effects and is purely dependent on the plenum pressurisation and the external aerodynamic forces. In this calculation, a COMSOL model (see Section II.D) is used where the plenum pressure is uniformly varied in magnitude and the respective principal stress fields are used to calculate the overall probability of failure (see Section II.E). For each case, the plenum pressure is converted into the corresponding coolant mass flux using a SLEDGE simulation (see Section II.C) of the porous domain.

The burst heat flux is defined as the heat flux magnitude, i.e. the stagnation point heat flux, that leads to a probability of failure of 1 %. A larger heat flux will lead to larger thermal stresses which will result in a higher probability of failure. A higher burst heat flux is obviously also desirable as this means that the particular architecture can withstand higher thermal loads and requires therefore less cooling. As a first step, the PIRATE tool (see Section II.A) is used to determine the aerodynamic heat flux distribution around the external surface of the leading edge. This distribution is then scaled to different magnitudes and used as a boundary condition for a COMSOL model (see Section II.D), in which the temperature and principal stress fields are calculated. The stress fields are subsequently used to determine the overall probability of failure using the Barnett–Freudenthal method (see Section II.E) for each individual case. The thermal loading case is also investigated in isolation in this study, i.e. without the effect of cooling or plenum pressurisation. The reasoning for de-coupling the interplay between thermally induced and mechanically induced stress is to identify whether certain types of geometries are prone to fail due to one of these aspects. A fully coupled analysis is conducted in Section V.

Figure 11 shows an example of the first principal stress distribution for a purely thermal load with a stagnation point heat flux magnitude of 7.6 $\mathrm{MW/m^2}$, and Figure 12 shows the first principal stress for a purely mechanical load of 20 bar in each plenum. The resulting probability of failure of these models for a variation of loading cases is shown in Fig 13. The respective burst mass- or heat flux is where the curves of each model cross the 1 % probability of failure level. It is clear from this graph that some configurations perform much better than others, as the amount of allowable heat flux or mass flux varies greatly from case to case, before the probability of failure becomes too large.

The resulting metrics are shown in more detail in Fig. 14 where a combination of plenum spacing and porous thickness are investigated. The closest plenum spacing is best for relieving thermal expansion and thus can withstand the largest heat flux value. Furthermore, it is shown that this geometry is also best for driving the largest mass flux through the leading edge before failing. Thus, the 0.4 mm $\times$ 0.4 mm (width $\times$ thickness) geometry clearly emerges as the best option. It is especially noteworthy that the geometries with larger porous thicknesses are worse in both metrics. Thicker structures lead to a large increase in stress due to the very high stiffness of the material and hence increase the probability of failure. Furthermore, a large influence of heat conduction is observed, where more material near the leading edge, i.e. close plenum spacing, leads to a relief of thermal stresses due to the increased heat conduction capability and therefore decreased thermal gradient. In the following, the closely spaced plenum geometry is taken

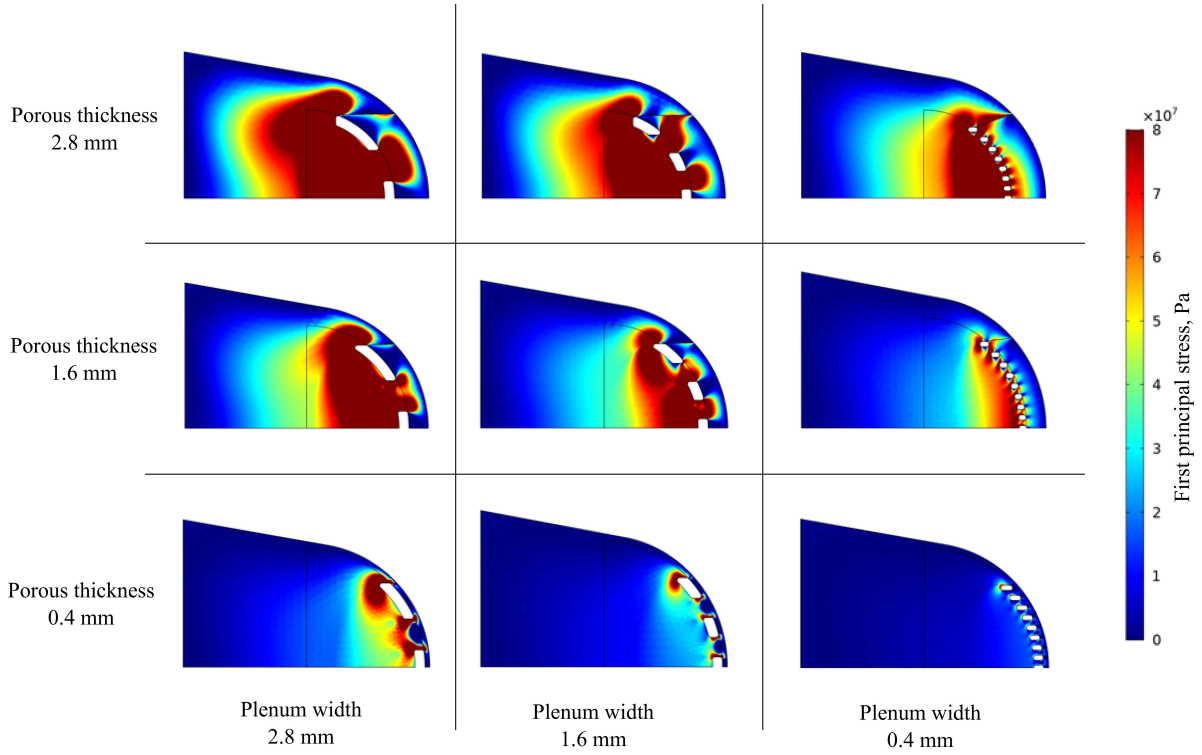

Fig. 11 First principal stress due to thermal expansion for a purely thermal load with a stagnation point heat flux magnitude of 7.6 MW/m^2.

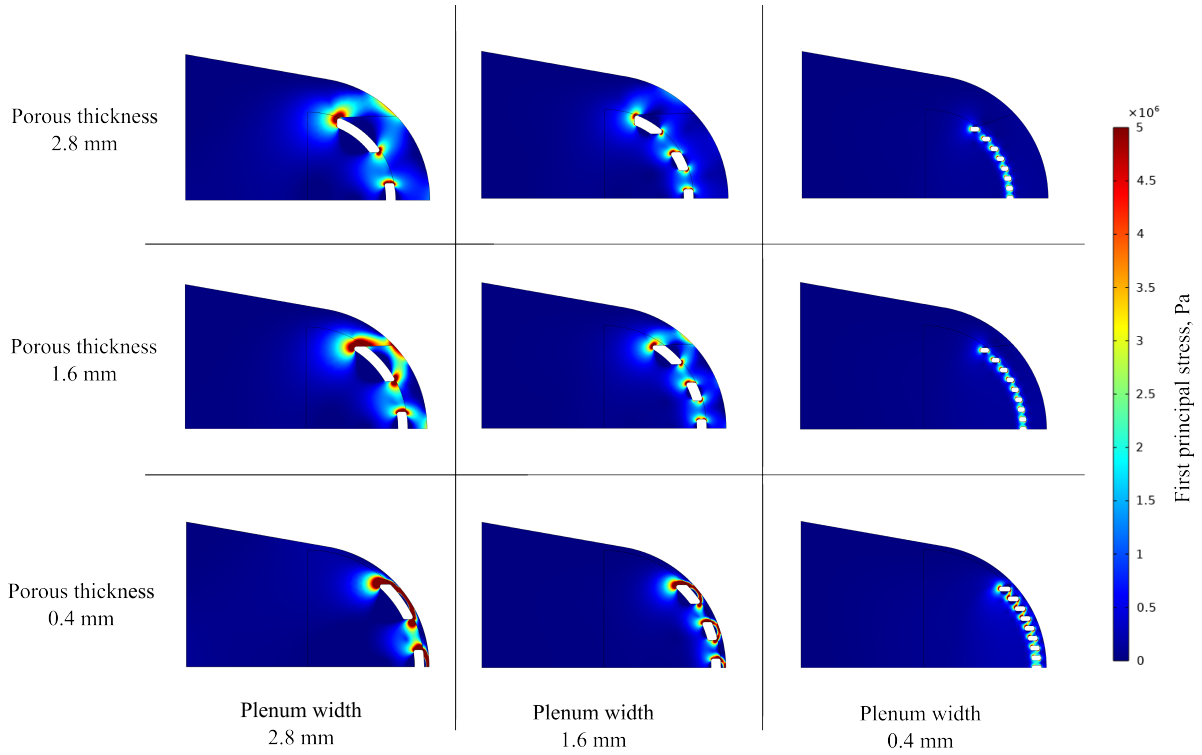

Fig. 12 First principal stress for a purely mechanical load of 20 bar in each plenum.

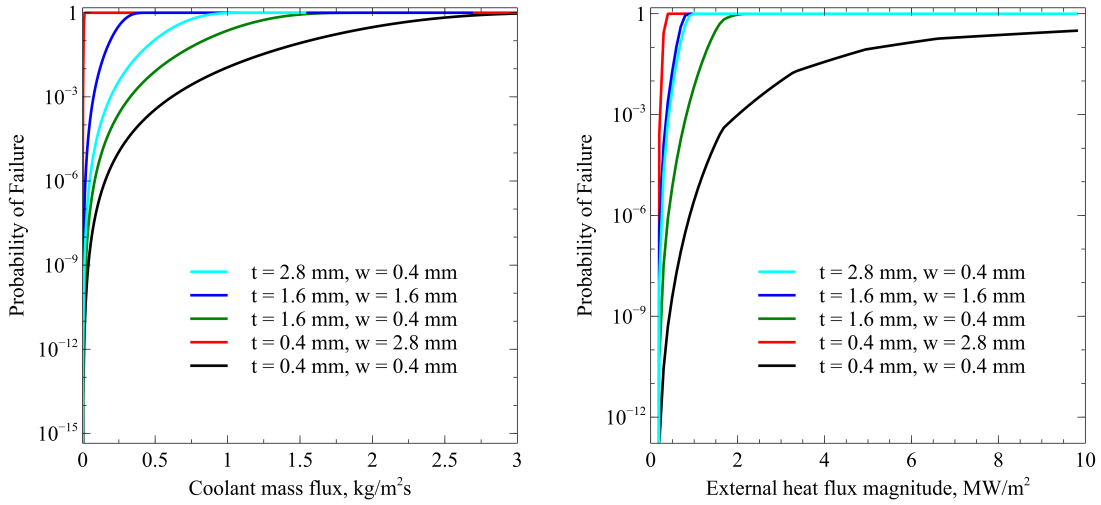

Fig. 13 Probability of failure for different magnitudes of coolant mass flux (left) and external heat flux (right). *t* **stands for the porous thickness and** *w* **stands for the plenum width.**

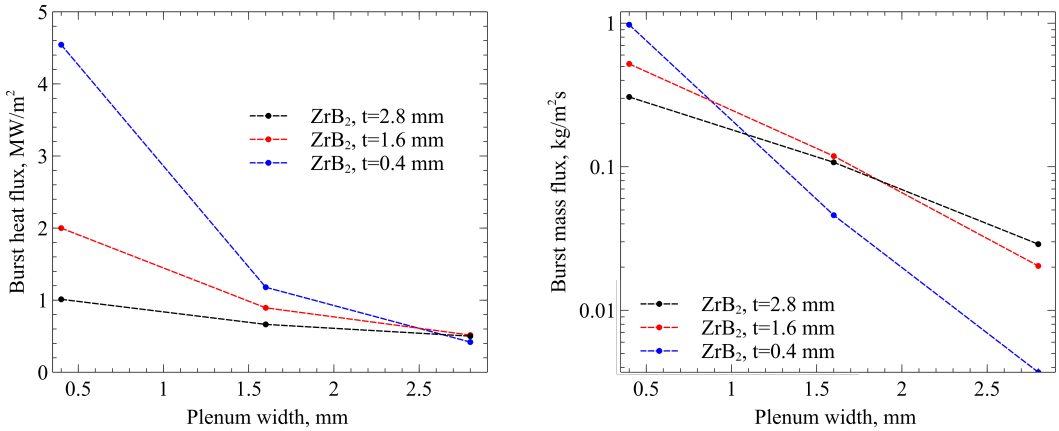

Fig. 14 Burst heat flux (left) and burst mass flux (right) as a function of the plenum spacing and the porous thickness.

forward and a more detailed analysis of its capability is employed.

V. Operational Corridor of Leading Edge

In this section, the methodology of an overall probability of failure is extended to account for the coupled effect of transpiration cooling, thermal stress, heat flux mitigation, and plenum pressurisation. In addition, the spatial coolant injection distribution is taken into account by optimising the pressure in each plenum. By taking the cooling effectiveness of different gas mass fluxes into account, it is found that there exists an optimum operating plenum pressure that minimizes the probability of failure. For this analysis, only the most promising geometries are employed, a plenum

spacing of 0.4 mm with two porous layer thicknesses, 0.4 mm and 1 mm. The full procedure of the optimisation process is described in Section II.

Four combinations are investigated: Nitrogen coolant with 0.4 mm porous thickness, Nitrogen coolant with 1 mm porous thickness, Helium coolant with 0.4 mm porous thickness, Helium coolant with 1 mm porous thickness. The resulting probability of failure for various plenum pressurisation cases is shown in Fig. 16 (left). An example of the stress distribution for one of those cases is shown in Fig. 15.

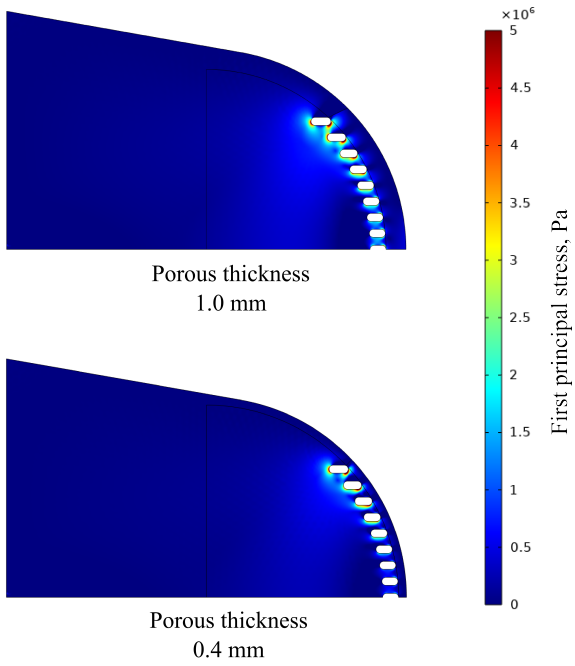

Fig. 15 First principal stress due to thermal expansion and plenum pressurisation for Helium coolant with maximum plenum pressure of 18.8 bar.

The probability of failure exhibits a minimum for all considered cases. For very low plenum pressures, insufficient cooling occurs and thermal stress dominates. This leads to a high probability of failure. As plenum pressures rise, the cooling efficiency increases, blocking more and more of the external heat flux. This reduces the thermal stress and hence reduces the probability of failure. As the plenum pressure is further increased, it introduces larger mechanical stresses which increase the overall probability of failure again. In between the thermal stress and mechanical stress dominated regions is the "sweet spot" where the leading edge can be operated safely.

Figure 16 shows that Helium coolant generally requires higher pressures to reduce the heat flux sufficiently, so that thermal stresses are mitigated. This is due to the low molecular weight of Helium which requires high pressures to drive sufficient coolant mass flux. This downside is not outweighed by its superior cooling efficiency, which is mostly driven by the large specific heat of Helium. Leading edges with a thinner porous layer show a wider operating space where the probability of failure is low. This can be explained by the lower resistance for the coolant flow, i.e. lower

plenum pressures are required to drive an adequate coolant mass flux leading to a reduction of the external net heat flux into the structure. Therefore, lower plenum pressures are required for $t = 400\,\mu$m to alleviate the thermal stress which dominates failure at low plenum pressure regions. Fig. 16 (right) shows the maximum air mass fraction at the wall for the same plenum pressure conditions which has been calculated using the methodology outlined in Section II.A.1. The figure shows that Nitrogen requires much less driving pressure to reduce the air concentration to a negligible amount, and thus preventing significant surface oxidation. Nitrogen has previously been identified as being superior to Helium in terms of freestream air displacement [31].

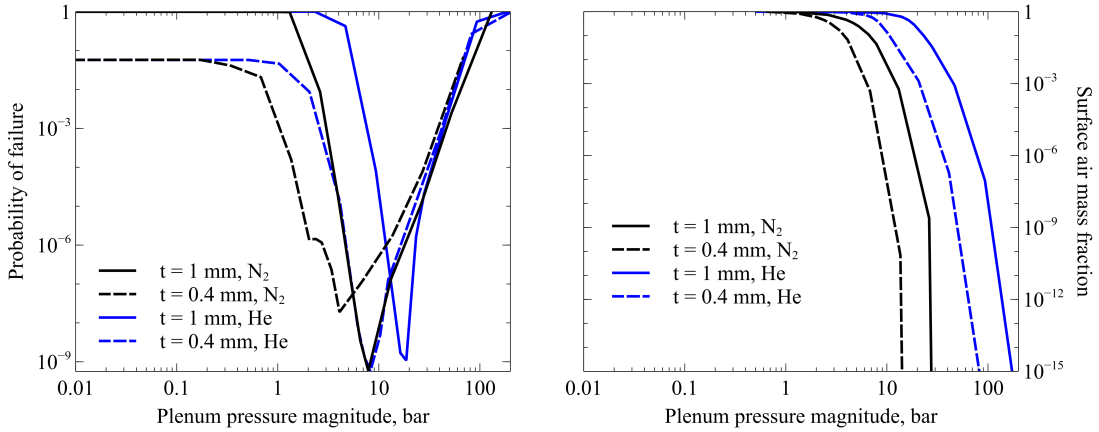

Fig. 16 Overall probability of failure (left) and maximum air mass fraction at the wall (right) using different coolants and porous thicknesses over plenum pressure magnitude.

Figure 17 gives a final comparison of all considered cases where the following assumptions have been made to simplify data interpretation: a maximum permissible probability of failure of 1% is allowed, and a maximum surface air mass fraction of 10^{-3} is allowed. The figure shows that in all cases, the minimum possible plenum pressure is dictated by air reaching the surface. If not sufficiently displaced by coolant gas, this would lead to oxidation and hence failure of the leading edge [31, 38]. The maximum possible plenum pressure is in a similar range for all studied geometries and lies between approximately 50–65 bar. The failure mechanism is predominantly driven by the mechanical stress due to plenum pressurisation. In conclusion, the best performing architecture is achieved by a thin porous layer utilising nitrogen coolant.

VI. Conclusion

This paper presents a numerical analysis of transpiration cooled sharp leading edges made from ultra-high-temperature ceramics. A number of simulation tools are employed that simulate the external aerodynamic effects with mass injection (PIRATE), the compressible flow through porous media (SLEDGE), the thermo-mechanical structural analysis (COMSOL), and a probabilistic structural model. The effect of catalytic heat flux reduction is taken into

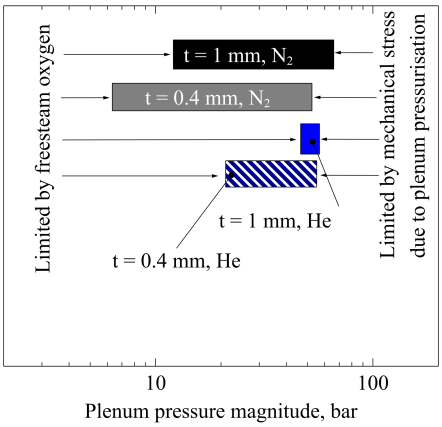

Fig. 17 Operational corridor for the considered cases, as a function of plenum pressure magnitude.

account by using empirical mixing correlations and a stagnation point injection model based on film theory. These models are used to simulate the entirety of a leading edge of 10 mm nose radius with a wedge angle of 10 degrees in a steady state flight at 45 km altitude and 5.5 km/s speed. Different plenum geometries are considered to introduce the coolant into a porous layer at the vehicle's surface. Plenum spacing and the thickness of the porous layer are varied and it is found that the thinnest porous layer and the closest plenum spacing lead to the best performance. This geometry provides the least susceptibility with regards to thermal stresses and can provide the largest coolant mass flux of all investigated cases. This geometric configuration is used in a further optimisation procedure where the plenum pressures inside the individual chambers are varied such that the optimal injection distribution at the vehicle's surface is obtained. The plenum pressure magnitude of this distribution is then varied and an overall probability of failure is calculated. It is shown that there exists an optimal plenum pressurisation that minimises the probability of failure in the leading edge. Furthermore, it is shown that the presence of freestream oxygen further restricts the operational corridor and limits the minimum coolant mass flux and minimum plenum pressure. The results show that Nitrogen requires less plenum pressure than Helium to achieve minimal probability of failure and offers a wider corridor of operability. In addition, Nitrogen coolant achieves a lower air surface concentration than Helium for the same plenum pressure. This study identified three key design aspects for transpiration cooled leading edges utilising ultra high temperature ceramics. 1) The maximum number of plenums should be utilised, leading to the smallest possible individual plenum size. 2) The minimum porous thickness should be used. 3) Nitrogen is a superior coolant fluid to Helium.

Disclaimer

The views, opinions and/or findings expressed are those of the authors and should not be interpreted as representing the official views or policies of the Department of Defense or the U.S. Government.

Acknowledgments

The authors would like to greatly acknowledge the funding of this work by DARPA under the MACH program (reference HR001119S0022) and the Engineering and Physical Sciences Research Council (reference EP/P000878/1).

References

[1] Anderson, J. D., *Hypersonic and High-Temperature Gas Dynamics, Second Edition*, American Institute of Aeronautics and Astronautics, 2006. https://doi.org/10.2514/4.861956.

[2] Kays, W., Crawford, M., Weigand, B., and McGraw–Hill, *Convective Heat and Mass Transfer, 4th ed*, McGraw–Hill, New York, 2005.

[3] A., F. J., and Riddell, F. R., "Theory of Stagnation Point Heat Transfer in Dissociated Air," *Journal of the Aerospace Sciences*, Vol. 25, 1958, pp. 73–85. https://doi.org/10.2514/8.7517, URL https://doi.org/10.2514/8.7517http://dx.doi.org/10.2514/8.7517.

[4] Böhrk, H., Dittert, C., Weihs, H., Thiele, T., and Gülhan, A., "Sharp Leading Edge at Hypersonic Flight: Modeling and Flight Measurement," *Journal of Spacecraft and Rockets*, Vol. 51, 2014, pp. 1753–1760. https://doi.org/10.2514/1.a32892, URL https://doi.org/10.2514/1.A32892http://dx.doi.org/10.2514/1.a32892.

[5] Kasen, S. D., "Thermal Management at Hypersonic Leading Edges," Ph.D. thesis, 2013.

[6] Modlin, J. M., and Colwell, G. T., "Surface cooling of scramjet engine inlets using heat pipe, transpiration, and film cooling," *Journal of Thermophysics and Heat Transfer*, Vol. 6, 1992, pp. 500–504. https://doi.org/10.2514/3.388, URL https://doi.org/10.2514/3.388http://dx.doi.org/10.2514/3.388.

[7] Goldstein, R. J., and Jabbari, M. Y., "Film cooling effectiveness with helium and refrigerant 12 injection into a supersonic flow," *AIAA Journal*, Vol. 8, 1970, pp. 2273–2274. https://doi.org/10.2514/3.6100, URL https://doi.org/10.2514/3.6100http://dx.doi.org/10.2514/3.6100.

[8] Boehrk, H., Piol, O., and Kuhn, M., "Heat Balance of a Transpiration-Cooled Heat Shield," *Journal of Thermophysics and Heat Transfer*, Vol. 24, 2010, pp. 581–588. https://doi.org/10.2514/1.47172, URL https://doi.org/10.2514/1.47172http://dx.doi.org/10.2514/1.47172.

[9] Hoseinzade, D., and Kim, I., "Multiobjective optimization of porous medium for efficient transpiration cooling of hypersonic vehicles using genetic algorithm," *Physics of Fluids*, Vol. 36, 2024. https://doi.org/10.1063/5.0215973.

[10] Hermann, T., and McGilvray, M., "Analytical solution of flows in porous media for transpiration cooling applications," *Journal of Fluid Mechanics*, Vol. 915, 2021, p. A38. https://doi.org/10.1017/jfm.2021.126.

[11] Saikia, B., and Brehm, C., "Effects of Transpiration Cooling on Hypersonic Boundary-Layer Receptivity and Stability for Blunt Cones," *AIAA AVIATION 2023 Forum*, American Institute of Aeronautics and Astronautics, 2023. https://doi.org/10.2514/6.2023-3673.

[12] Kerth, P., Page, L. M. L., Wylie, S., Ravichandran, R., Ceruzzi, A., Williams, B. A. O., and McGilvray, M., "Displacement of hypersonic boundary layer instability and turbulence through transpiration cooling," *Physics of Fluids*, Vol. 36, 2024. https://doi.org/10.1063/5.0189321.

[13] Cerminara, A., Nayak, R., Potts, J., Tanno, H., Kloker, M. J., Saikia, B., Brehm, C., Camillo, G. P., and Wagner, A., "Transpiration cooling in hypersonic flow and mutual effect on turbulent transition and cooling performance," *Physics of Fluids*, Vol. 37, 2025. https://doi.org/10.1063/5.0253164.

[14] Martino, G. D. D., Peichl, J., Hufgard, F., Duernhofer, C., Loehle, S., and Göser, J., "Main flight data on transpiration cooled sharp edge fins in hypersonic conditions on the sounding rocket HIFLIER," *Aerospace Science and Technology*, Vol. 158, 2025, p. 109895. https://doi.org/10.1016/j.ast.2024.109895.

[15] Feilden, E., Blanca, E. G.-T., Giuliani, F., Saiz, E., and Vandeperre, L., "Robocasting of structural ceramic parts with hydrogel inks," *Journal of the European Ceramic Society*, Vol. 36, 2016, pp. 2525–2533. https://doi.org/10.1016/j.jeurceramsoc.2016.03.001.

[16] Naved, I., Hermann, T., and McGilvray, M., "Numerical Simulation of Transpiration Cooling for a High-Speed Vehicle with Substructure," *AIAA Journal*, 2021, pp. 1–12. https://doi.org/10.2514/1.j059771, URL https://doi.org/10.2514/1.J059771http://dx.doi.org/10.2514/1.j059771.

[17] Hermann, T., McGilvray, M., Williams, B., Wylie, S., Hambidge, C., Penty-Geraets, R., Bucknell, A., Doherty, L., and Ewart, E., *Total Temperature Measurements in the Oxford High Density Tunnel*, 2019. Submitted.

[18] Hermann, T., Naved, I., and McGilvray, M., "Tool for Rapid Transient Transpiration-Cooled Reentry Simulation," *AIAA Journal*, Vol. 58, 2020, pp. 842–853. https://doi.org/10.2514/1.J058516.

[19] Sutton, K., and Graves, R., "A general stagnation-point convective heating equation for arbitrary gas mixtures," Tech. rep., 1971.

[20] McBride, B. J., and Gordon, S., "Computer Program for Calculation of Complex Chemical Equilibrium Compositions and Applications," Tech. rep., NASA Reference Publication 1311, 1996.

[21] Lees, L., "Laminar Heat Transfer Over Blunt-Nosed Bodies at Hypersonic Flight Speeds," *Journal of Jet Propulsion*, Vol. 26, 1956, pp. 259–269. https://doi.org/10.2514/8.6977, URL https://doi.org/10.2514/8.6977http://dx.doi.org/10.2514/8.6977.

[22] Volchkov, E. P., Zaulichnyi, E. G., Kutateladze, S. S., and Leont'ev, A. I., "Film cooling by injection into a turbulent boundary layer," *Journal of Applied Mechanics and Technical Physics*, Vol. 8, 1967, pp. 63–64. https://doi.org/10.1007/BF00918038, URL https://doi.org/10.1007/BF00918038http://dx.doi.org/10.1007/BF00918038.

[23] Sellers, J. P., "Gaseous Film Cooling with Multiple Injection Stations," *AIAA Journal*, Vol. 1, 1963, pp. 2154–2156. https://doi.org/10.2514/3.2014, URL https://doi.org/10.2514/3.2014http://dx.doi.org/10.2514/3.2014.

[24] Rocher, M. E., Hermann, T., McGilvray, M., and Gollan, R., "Correlation for Species Concentration on a Hypersonic Stagnation Point with Mass Injection," *AIAA Journal*, Vol. 60, 2022, pp. 2798–2809. https://doi.org/10.2514/1.J061159.

[25] Hermann, T., and McGilvray, M., "Analytical solution of flows in porous media for transpiration cooling applications," *Journal of Fluid Mechanics*, Vol. 915, 2021, p. A38. https://doi.org/10.1017/jfm.2021.126, URL http://dx.doi.org/10.1017/jfm.2021.126https://www.cambridge.org/core/article/analytical-solution-of-flows-in-porous-media-for-transpiration-cooling-applications/CF971A9BA560907215585951489B62C6.

[26] Dittert, C., Selzer, M., and Böhrk, H., "Flowfield and Pressure Decay Analysis of Porous Cones," *AIAA Journal*, Vol. 55, 2018, pp. 874–882. https://doi.org/10.2514/1.j055298, URL https://doi.org/10.2514/1.J055298http://dx.doi.org/10.2514/1.j055298.

[27] J. D., A., *Computational Fluid Dynamics - The Basics with Applications*, McGraw-Hill series in aeronautical and aerospace engineering, 1995.

[28] Nemeth, N. N., Jadaan, O. M., Palfi, T., and Baker, E. H., "Predicting the Reliability of Ceramics Under Transient Loads and Temperatures with CARES/Life," *Journal of ASTM International*, Vol. 1, 2004, pp. 1–19. URL https://www.astm.org/DIGITAL_LIBRARY/JOURNALS/JAI/PAGES/JAI11578.htm.

[29] Rizvi, S., Linshu, H., Dajun, X., and Shah, S., "Trajectory optimisation for a rocket-assisted hypersonic boost-glide vehicle," *The Aeronautical Journal*, Vol. 121, 2017, pp. 469–487. https://doi.org/10.1017/aer.2017.11.

[30] Ifti, H. S., Hermann, T., and McGilvray, M., "Analytical Model of Transpired-Coolant Concentration at Downstream Wall in High-Speed Laminar Flow," *AIAA Journal*, Vol. 61, 2023, pp. 3541–3550. https://doi.org/10.2514/1.J062199.

[31] Rocher, M. E., Hermann, T., and McGilvray, M., "Oxidation Response of Transpiration-Cooled ZrB2 on a Hypersonic Stagnation Point," *Journal of Spacecraft and Rockets*, Vol. 59, 2022, pp. 1486–1495. https://doi.org/10.2514/1.A35309.

[32] Chase, M. W., of Standards, N. I., and (u.s.), T., *NIST-JANAF thermochemical tables*, American Chemical Society ; American Institute of Physics for the National Institute of Standards and Technology, 1998.

[33] Ifti, H. S., Hermann, T., and McGilvray, M., "Flow Characterisation of Transpiring Porous Media for Hypersonic Vehicles," *22nd AIAA International Space Planes and Hypersonics Systems and Technologies Conference*, American Institute of Aeronautics and Astronautics, 2018. https://doi.org/10.2514/6.2018-5167.

[34] Balat-Pichelin, M., Bêche, E., Sciti, D., and Alfano, D., "Emissivity, catalycity and microstructural characterization of ZrB2-SiCfiber based UHTC at high temperature in a non-equilibrium air plasma flow," *Ceramics International*, Vol. 40, 2014, pp. 9731–9742. URL http://www.sciencedirect.com/science/article/pii/S0272884214002582.

[35] Prikhna, T. O., Lokatkina, A. S., Barvitskyi, P. P., Karpets, M. V., Ponomaryov, S. S., Bondar, A. A., Büchner, B., Werner, J., Kluge, R., Moshchil, V. E., Borymskyi, O. I., Devin, L. M., Rychev, S. V., Haber, R., Yasar, Z. A., Matovic, B., Rucki, M., and Prisyazhna, O. V., "Structure, Mechanical Properties, and High-Temperature Stability of ZrB2- and HfB2-Based Materials," *Journal of Superhard Materials*, Vol. 45, 2023, pp. 321–335. https://doi.org/10.3103/S1063457623050076.

[36] Zhang, J., and McMahon, J. M., "Temperature-dependent mechanical properties of ZrC and HfC from first principles," *Journal of Materials Science*, Vol. 56, 2021, pp. 4266–4279. https://doi.org/10.1007/s10853-020-05416-6.

[37] Tiwari, J., and Feng, T., "Intrinsic thermal conductivity of ZrC from low to ultrahigh temperatures: A critical revisit," *Physical Review Materials*, Vol. 7, 2023, p. 065001. https://doi.org/10.1103/PhysRevMaterials.7.065001.

[38] Rocher, M. E., McGilvray, M., Hermann, T. A., Ifti, H. S., Hufgard, F., Eberhart, M. F., Meindl, A., Loehle, S., Giovannini, T., and Vandeperre, L. J., "Testing a Transpiration Cooled Zirconium-Di-Boride sample in the Plasma Tunnel at IRS," *AIAA Scitech 2019 Forum*, American Institute of Aeronautics and Astronautics, 2019. https://doi.org/10.2514/6.2019-1552.